Knowledge-Based Systems 216 (2021) 106657

Contents lists available at ScienceDirect

Knowledge-Based Systems

journal homepage: www.elsevier.com/locate/knosys

Endmember independence constrained hyperspectral unmixing via nonnegative tensor factorization

Jin-Ju Wang, Ding-Cheng Wang, Ting-Zhu Huang *, Jie Huang *, Xi-Le Zhao, Liang-Jian Deng

School of Mathematical Sciences, University of Electronic Science and Technology of China, Chengdu, Sichuan, 611731, PR China

ARTICLE INFO

Article history:
Received 4 July 2020
Received in revised form 4 December 2020
Accepted 5 December 2020
Available online 23 January 2021

Keywords:
Hyperspectral unmixing
Low-rankness
Endmember independence constraint
Nonnegative tensor factorization (NTF)

ABSTRACT

Hyperspectral unmixing is an essential step for the application of hyperspectral images (HSIs), which estimates endmembers and their corresponding abundances. In recent decades, nonnegative matrix factorization (NMF) and nonnegative tensor factorization (NTF) have been widely exploited for hyperspectral unmixing. To improve the unmixing performance, various constraints have been applied in many NMF-based and NTF-based methods. Though many regularizations are used to describe abundances' properties, less attention is paid to endmember signatures. Notice that, endmember information is important for obtaining accurate estimated endmembers from the highly correlated spectral signatures in HSIs. Thus, constraints on both endmembers and abundances are expected to make spectral signatures separated adequately. In this paper, we propose a new NTF-based model, termed as endmember independence constrained hyperspectral unmixing via NTF (EIC-NTF). It aims to mitigate the impact of high correlation among spectral signatures from endmembers and abundances. For endmember estimation, we introduce an endmember independence constraint to avoid obtaining similar endmembers estimations. For abundance estimation, we exploit the low-rankness in abundance maps to describe the spatial correlation of mixed pixels lying in homogeneous regions of HSIs. We solve the proposed model under the augmented multiplicative update framework. Experimental results on both synthetic and real hyperspectral data demonstrate that the proposed algorithm is effective for hyperspectral unmixing.

1. Introduction

Hyperspectral images (HSIs) not only contain spatial information but a large amount of spectral information. Thus they have been widely used in many fields, such as target detection and classification [1–4]. Due to the low spatial resolution and the complex distribution of ground features, an HSI contains plenty of mixed pixels, whose spectral signatures are composed of several pure substances (endmembers) [5]. The existence of mixed pixels increases the difficulty of applying HSIs. Therefore, hyperspectral unmixing, decomposing a mixed pixel into several endmembers and its corresponding fractions (abundances), plays an important role in HSIs processing [6–8].

Recall that a mixed pixel is the result of a mixing process, thus, the type of mixing is critical for hyperspectral unmixing. Due to the simplicity and applicability of the linear mixing model (LMM), it is applied in many unmixing algorithms [6,9–11]. Under the LMM, a mixed pixel is a linear combination of the endmembers, proportioned by their corresponding abundances [12]. Usually, the abundances meet two physical constraints: the abundance nonnegative constraint (ANC) and the abundance sum-to-one constraint (ASC).

Based on LMM, many unmixing strategies have been proposed, ranging from endmember determination to a semi-supervised strategy [9,13–16]. Endmember determination methods, such as Pixel Purity Index (PPI) [17], N-FINDR [18], and Vertex Component Analysis (VCA) [13], are used to estimate endmembers. They assume that pure pixels exist in an HSI, which is rather strict in some practical situations. For the semi-supervised strategy based methods, they need the endmembers in an HSI or a library including all endmembers in advance.

When endmembers in an HSI are unavailable, unmixing problems are transformed as blind source separation (BSS) problems. To tackle BSS, nonnegative matrix factorization (NMF) and its extensions have been introduced for hyperspectral unmixing [19–22]. The NMF-based methods decompose a 3-D HSI into a 2-D matrix approximated by the product of two nonnegative matrices. One nonnegative matrix denotes the material endmembers and the other represents the related abundances [23,24]. According to the data analysis, NMF provides a part-based representation

* Corresponding authors.
E-mail addresses: tingzhuhuang@126.com (T.- Z. Huang), huangjie_uestc@uestc.edu.cn (J. Huang).

https://doi.org/10.1016/j.knosys.2020.106657
0950-7051/

of the data [25]. Unfortunately, these NMF-based methods are nonconvex, which is hard to avoid the existence of local minima. A popular method to overcome this drawback is by introducing additional constraints into NMF according to the priors of HSIs. Usually, sparse constraint with ℓ_q norm is incorporated into NMF to enhance the sparsity of the abundance matrix [21,22,26]. In addition, spatial information among pixels is also exploited in many NMF-based algorithms [10,27–29]. With the popularity of the deep learning strategy, many deep learning-based unmixing approaches have been proposed for the unmixing process to achieve powerful and flexible feature representations [30–33]. They provide more accurate unmixing results. Considering the run-time and accuracy of the HSI unmixing process, we concentrate on studying traditional unmixing models in this paper.

Even NMF models achieve promising unmixing results, they miss a lot of spectral and spatial information when decomposing a 3-D data into a 2-D matrix [34]. To remain more image information, Qian et al. [34] introduce a matrix–vector nonnegative tensor factorization (MV-NTF) model. They view a 3-D HSI as the sum of several tensors, which is the outer product of a matrix (abundance map) and a vector (endmember signature). Besides, they also impose the low-rank structure on each abundance map with the product of two low-rank matrices. The framework of MV-NTF is consistent with the LMM and catches the intrinsic structure of the HSI. To relive the effect of noise, Feng et al. propose an algorithm called total variation (TV) regularized MV-NTF [MV-NTF-TV] [35]. MV-NTF-TV incorporates the TV term into the framework of MV-NTF to suppress the noise and decrease the number of local minima. At the same time, TV adaptively promotes piecewise smoothness while preserving edges [36]. Generally, these MV-NTF based methods behave better than NMF-based methods for hyperspectral unmixing. However, the forceful low-rank constraint on abundance maps may limit the representation of some details in HSI. Moreover, MV-NTF based methods lack guarantees that mixed spectral signatures separate adequately. In other words, some endmembers obtained by MV-NTF may be similar.

In this paper, we propose an algorithm named endmember independence constrained hyperspectral unmixing via nonnegative tensor factorization (EIC-NTF). The proposed EIC-NTF method considers an endmember independence constraint and the low-rank structure of each abundance map to alleviate the high correlation among spectral signatures. The framework of EIC-NTF is shown in Fig. 1. First, an HSI is decomposed into the sum of the outer product of endmembers and their related abundance maps. Then, applying the endmember independence constraint on the endmembers and the low-rank constraint on each abundance map, we obtain the smooth endmember signatures and the low-rank abundance maps. Finally, we update the abundance maps and endmembers with the above results in each iteration until meeting the stop condition. Experiments on both synthetic and real data have shown the advantages of our method over several state-of-the-art approaches. The main contributions of this paper are:

1. According to LMM, endmembers are different and linear independent from each other. To relieve the high correlation between spectral signatures, we introduce an endmember independence constraint to remain the feature of the endmember signatures and constrain them to be smooth.
2. Recall that NTF-based methods consider a natural representation of an HSI, it avoids information loss when decomposing a 3-D data into a 2-D matrix. We formulate the proposed method based on the NTF model. Different from the fixed rank of each abundance map in MV-NTF, we describe the low-rankness of each abundance map with the weighted nuclear norm. The weighted nuclear norm treats each abundance map differently.

The rest of this paper is organized as follows. Section 2 briefly introduces tensor basis, LMM, and the NTF model. Section 3 shows the details of the proposed model, the associated update rules. The experimental results on synthetic data are presented and analyzed in Section 4. In Section 5, real-data experiments are conducted. Finally, conclusions and future work are given in Section 6.

2. Background and notations

This section will introduce some basic concepts about tensor to link the nonnegative tensor factorization and hyperspectral unmixing. We then present the LMM model and how the LMM is applied in hyperspectral unmixing.

2.1. Tensor notations and concepts

A tensor is a multidimensional array [37]. The N-th order tensor denotes a tensor which contains N dimensions, and each dimensionality has its coordinate system. In this paper, scalars, tensors of order zero, are denoted by lowercase letters, e.g., y. Vectors, first-order tensors, are denoted by boldface lowercase letters, e.g., $\mathbf{y} \in \mathbb{R}^I$. Matrices, second-order tensors, are denoted by boldface capital letters, e.g., $\mathbf{Y} \in \mathbb{R}^{I\times J}$. Higher-order tensors, tensors of order three or higher, are represented by boldface Euler script letters, e.g., $\mathcal{Y} \in \mathbb{R}^{I_1\times I_2\times\cdots\times I_N}$.

Definition of the Matricization: Matricization transforms a tensor into a matrix. Specifically, the mode-n matricization of a tensor $\mathcal{X} \in \mathbb{R}^{I_1\times I_2\cdots\times I_N}$ reorders the mode-n arrays to be the columns of the resulting matrix, which is denoted by $\mathcal{X}_{(n)}$. Taken a third-order tensor $\mathcal{Y} \in \mathbb{R}^{I\times J\times L}$ as an example, it can be unfolded in three ways according to its three mode arrays, respectively,

$$\begin{aligned}\left(\mathbf{Y}_{(1)}\right)(j-1)L+l,i &= y_{ijl}\\ \left(\mathbf{Y}_{(2)}\right)(l-1)I+i,j &= y_{ijl}\\ \left(\mathbf{Y}_{(3)}\right)(i-1)J+j,l &= y_{ijl}.\end{aligned}$$

Definition of the Outer Product: Given K vectors $\mathbf{b}^{(i)} \in \mathbb{R}^{\mathbf{N}_i}, i = 1,\ldots,K$, the outer product between them is a tensor $\mathcal{X} = \mathbf{b}^{(1)}\circ\mathbf{b}^{(2)}\circ\cdots\circ\mathbf{b}^{(K)} \in \mathbb{R}^{\mathbf{N}_1\times\mathbf{N}_2\times\cdots\times\mathbf{N}_K}$. Each element of the tensor $\mathcal{X}$ is the product of the corresponding vector elements:

$$x_{i_1 i_2\cdots i_R} = b^{(1)}_{i_1}\times b^{(2)}_{i_2}\cdots b^{(K)}_{i_K} \quad \text{for all} \quad 1\le i_n\le \mathbf{N}_i$$

Definition of the Kronecker Product and Khatri–Rao Product: Given two matrices $\mathbf{A} \in \mathbb{R}^{I\times J}, \mathbf{B} \in \mathbb{R}^{K\times L}$, their Kronecker product, $\mathbf{A}\otimes\mathbf{B} \in \mathbb{R}^{(IK)\times(JL)}$, is defined by

$$\mathbf{A}\otimes\mathbf{B} = \begin{pmatrix} a_{11}\mathbf{B} & a_{12}\mathbf{B} & \cdots & a_{1J}\mathbf{B}\\ a_{21}\mathbf{B} & a_{22}\mathbf{B} & \cdots & a_{2J}\mathbf{B}\\ \vdots & \vdots & \ddots & \vdots\\ a_{I1}\mathbf{B} & a_{I2}\mathbf{B} & \cdots & a_{IJ}\mathbf{B}\end{pmatrix}$$
$$= [\mathbf{a}_1\otimes\mathbf{b}_1 \;\; \mathbf{a}_1\otimes\mathbf{b}_2 \;\; \mathbf{a}_1\otimes\mathbf{b}_3\cdots\mathbf{a}_J\otimes\mathbf{b}_{L-1} \;\; \mathbf{a}_J\otimes\mathbf{b}_L],$$

where $\mathbf{a}_j$ $(j = 1,2,\ldots,J)$ denotes the jth column in $\mathbf{A}$, $\mathbf{a}_{ij}$ denotes the element (i,j) of $\mathbf{A}$. A similar denotation is as $\mathbf{B}$.

When $\mathbf{A}$ and $\mathbf{B}$ have the same number of columns, i.e., $J = L$, their Khatri–Rao product $\mathbf{A}\odot\mathbf{B} \in \mathbb{R}^{(IK)\times J}$, is denoted by

$$\mathbf{A}\odot\mathbf{B} = [\mathbf{a}_1\otimes\mathbf{b}_1 \;\; \mathbf{a}_2\otimes\mathbf{b}_2 \;\; \cdots \;\; \mathbf{a}_J\otimes\mathbf{b}_J].$$

When $\mathbf{A} = [\mathbf{A}_1\cdots\mathbf{A}_R]$ and $\mathbf{B} = [\mathbf{B}_1\cdots\mathbf{B}_R]$ are two block matrices with the same number of submatrices, the generalized Khatri–Rao product for partitioned matrices is

$$\mathbf{A}\bar{\odot}\mathbf{B} = [\mathbf{A}_1\odot\mathbf{B}_1 \;\; \mathbf{A}_2\odot\mathbf{B}_2 \;\; \cdots \;\; \mathbf{A}_R\odot\mathbf{B}_R].$$

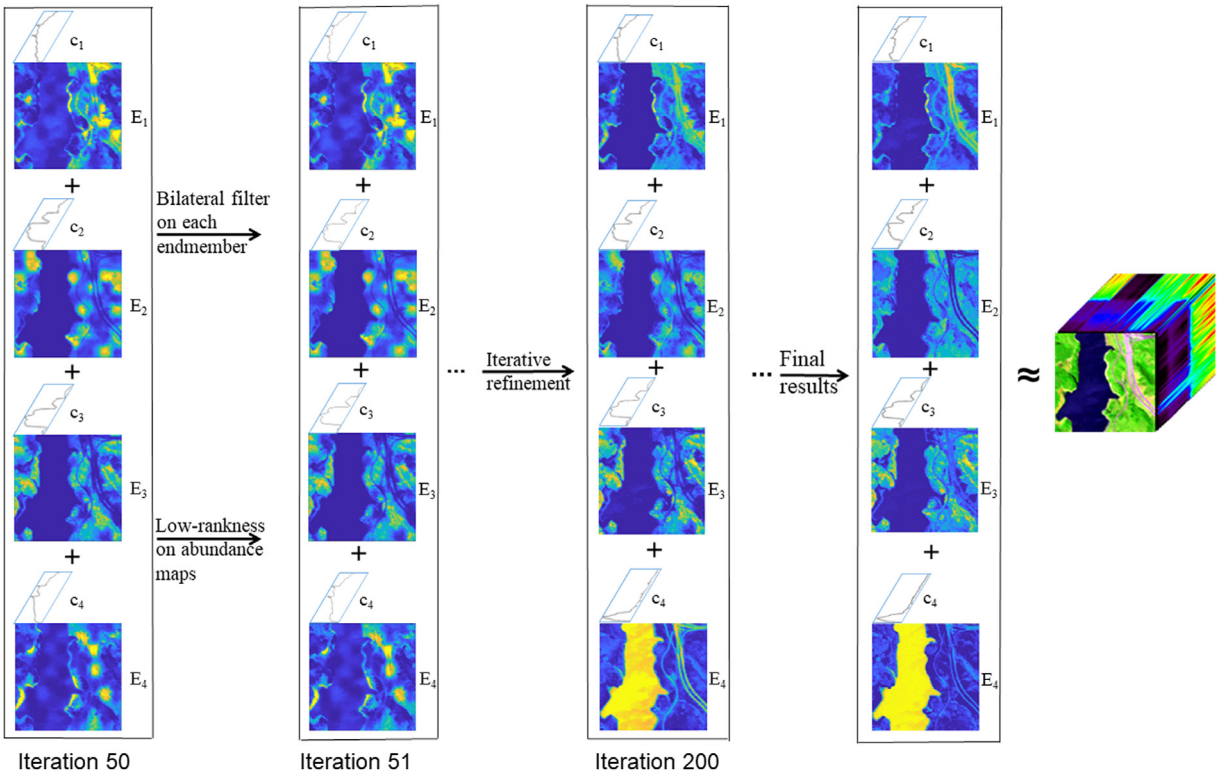

Fig. 1. Framework of the proposed method. At first, the given HSI is decomposed into the sum of the outer product of endmembers $\mathbf{c}_r$ and abundance maps $\mathbf{E}_r$. Then, the endmember constraint and the low-rank constraint are imposed on endmember signatures and each abundance map respectively, leading to relatively independent endmember signatures and the low-rank abundance maps. The spectral and spatial information is fed back to the next iteration of a tensor factorization to improve the results iteratively. Finally, the proposed method provides independent endmembers and low-rank abundance maps.

2.2. LMM

Given an HSI $\mathcal{Y} \in \mathbb{R}^{I\times J\times L}$, containing $I \times J$ pixels with L bands. And $\mathbf{y}_i \in \mathbb{R}^L$ is the ith mixed pixel. The LMM [6] expresses it as

$$\begin{aligned} &\mathbf{y}_i = \mathbf{C}\mathbf{s}_i + \alpha_i, \\ &s.t.\ \mathbf{1}^T\mathbf{s}_i = 1, \mathbf{s}_i \geq \mathbf{0}, \end{aligned} \tag{1}$$

where $\mathbf{C} = [\mathbf{c}_1 \cdots \mathbf{c}_R] \in \mathbb{R}^{L\times R}$, $\mathbf{c}_i \in \mathbb{R}^{L\times 1}$ denotes the ith endmember, $\mathbf{s}_i \in \mathbb{R}^R$ is a vector of abundance fractions for each endmember, and α_i is an additive white Gaussian noise. Here, $\mathbf{1} \in \mathbb{R}^{R\times 1}$ is a vector whose all elements are one. In Eq. (1), $\mathbf{s}_i \geq \mathbf{0}$ in (1) is the ANC and $\mathbf{1}^T\mathbf{s}_i = 1$ in (1) is the ASC.

For the classical NMF, an HSI, $\mathcal{Y} \in \mathbb{R}^{I\times J\times L}$ is unfolded corresponding to its mode-3 vectors. Then, the unmixing model according to LMM is written as

$$\mathbf{Y}_{(3)} = \mathbf{C}\mathbf{S} + \alpha,$$

where $\mathbf{Y}_{(3)} \in \mathbb{R}^{L\times(IJ)}$ contains $I \times J$ pixels with L bands, $\mathbf{S} = [\mathbf{s}_1\ \mathbf{s}_2 \cdots \mathbf{s}_{IJ}]$, and $\alpha = [\alpha_1\ \alpha_2\ \cdots\ \alpha_{IJ}]$. And, the corresponding loss function of NMF is considered as

$$\min_{\mathbf{C},\mathbf{S}} \frac{1}{2}\|\mathbf{Y}_{(3)} - \mathbf{C}\mathbf{S}\|_F^2,$$

where $\|\cdot\|_F$ denotes the Frobenius norm.

To enhance the sparsity of the abundance maps, Qian et al. incorporate the $L_{1/2}$ regularization into NMF, named $L_{1/2}$-NMF. This objective function is the combination of the reconstruction error and the $L_{1/2}$ regularization as follows

$$\min_{\mathbf{C},\mathbf{S}} \frac{1}{2}\|\mathbf{Y}_{(3)} - \mathbf{C}\mathbf{S}\|_F^2 + \lambda\|\mathbf{S}\|_{1/2},$$

where $\lambda \in \mathbb{R}^+$ is a scalar that weights the contribution of the $L_{1/2}$ regularization.

As described above, though NMF methods obtain great performance, they fail to fully preserve the spatial positions of pixels in the row indices, which is unavoidable to cause information loss [34]. Considering this situation, Qian et al. propose an MV-NTF model that regards an HSI as a 3-D tensor. This approach decomposes the observed 3-D HSI into the sum of R component tensors, where each one is factorized as the outer product of a matrix and a vector, representing abundance and endmember, respectively [34]. As illustrated in [34], MV-NTF is entirely consistent with the LMM. Mathematically, it can be formulated as

$$\mathcal{Y} = \sum_{r=1}^{R} \mathbf{A}_r\mathbf{B}_r^T \circ \mathbf{c}_r + \boldsymbol{\alpha} = \sum_{r=1}^{R} \mathbf{E}_r \circ \mathbf{c}_r + \boldsymbol{\alpha}, \tag{2}$$

where $\mathbf{E}_r \in \mathbb{R}^{I\times J}$ is the abundance map corresponding to the rth endmember, approximately represented by two low-rank matrices $\mathbf{A}_r$ and $\mathbf{B}_r$, $\mathbf{c}_r$ is the rth endmember. By incorporating the ASC constraint, Eq. (2) becomes minimizing the reconstruction error between $\mathcal{Y}$ and its R component tensors, which is represented by

$$\min_{\mathbf{A},\mathbf{B},\mathbf{C}} \frac{1}{2}\|\mathcal{Y} - \sum_{r=1}^{R} \mathbf{A}_r\mathbf{B}_r^T \circ \mathbf{c}_r\|_F^2 + \frac{\delta}{2}\|1_{I\times J} - \mathbf{A}\mathbf{B}^T\|_F^2, \tag{3}$$

where $\mathbf{1}_{I\times J}$ is a matrix of all ones and $\delta \in \mathbb{R}^+$ controls the balance between the reconstruction error and the ASC.

Treating the HSI as a whole tensor, MV-NTF takes advantage of 3-D information contained in an HSI. To exploit the local piecewise smoothness of the abundance maps and suppress the effect of noise, the TV regularization is imposed on MV-NTF in [35].

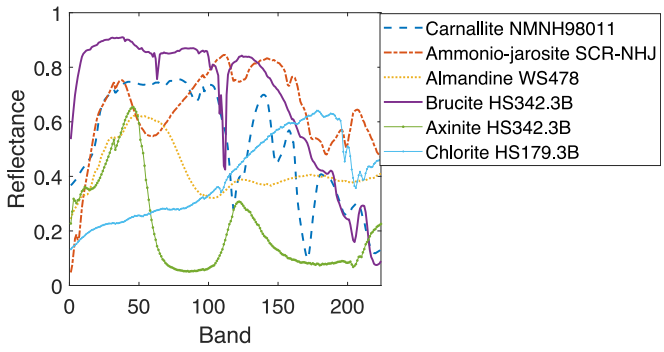

Fig. 2. Spectral signatures of six endmembers in USGS digital spectral library.

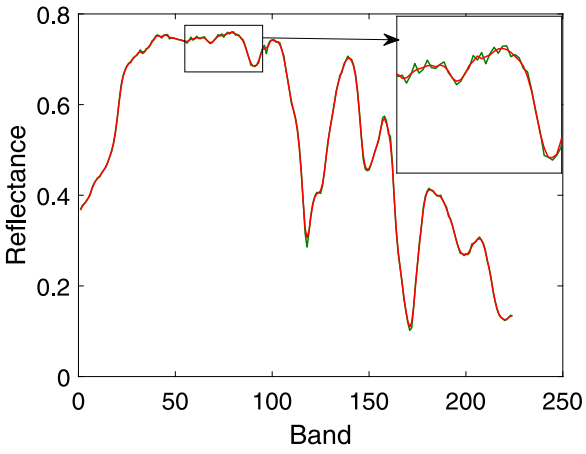

Fig. 3. The signature of endmember Carnallite corrupted by noise and the recovered endmember Carnallite by BF, the green line denotes endmember Carnallite corrupted by noise and the red line denotes recovered endmember Carnallite by BF.

3. The proposed EIC-NTF algorithm

In this section, we first introduce the crucial components of the proposed model, and then present the proposed model and the corresponding algorithm.

3.1. Endmember independence constraint

Recall that both endmembers and the corresponding abundances are the goals of hyperspectral unmixing, thus endmember signature constraints are also taken into account in the unmixing process. To analyze the endmember signatures, in Fig. 2, we show six endmembers (Carnallite, Ammonio-jarosite, Almandine, Brucite, Axinite, and Chlonte), which are from the United States Geological Survey (USGS) digital spectral library [38]. The selected spectral signatures contain 224 spectral bands with wavelengths from 0.38 to 2.5 μm.

According to Fig. 2, each endmember is independent of others, which is consistent with the assumption of LMM. In practice, the endmember signatures in HSIs are highly mixed and the spectral curves to be decomposed are highly correlated [39]. In this case, utilizing the spatial information is hard to guarantee that the spectral curves are separated adequately. To achieve accurate endmember curves, we introduce a new endmember independence constraint for endmember signatures. Recall that the bilateral filter is a popular image processing technique, which simultaneously preserves the edge and smooths the homogeneous region [40]. To present a more intuitive illustration, we show endmember Carnallite corrupted by noise and the recovered endmember Carnallite by the bilateral filter in Fig. 3. From Fig. 3, we observe that BF retains most of the spectral information and smoothes the endmember signature. Thus, we utilize the bilateral filter (BF) to capture these endmembers' features and constrain them to be smooth. Based on BF, we introduce an endmember signature constraint defined as follows

$$g(\mathbf{C}) = \|\mathbf{C}. * \mathbf{W}\|_F^2, \tag{4}$$

where $.*$ denotes the element-wise product. Here, $\mathbf{W} = [\mathbf{w}_1, \ldots, \mathbf{w}_R]$ is a weighting matrix, its ith column $\mathbf{w}_i$ is defined as

$$\mathbf{w}_i = 1./(\mathrm{BF}(\mathbf{c}_i) + \eta) \quad , \ i = 1, \ldots, R,$$

where BF is the bilateral filter, $./$ denotes the element-wise division, and η is a small value.

3.2. Low-rank approximation

Low-rank approximation, which aims to recover the underlying low-rank matrix from its degraded data, has been widely used in computer vision and machine learning [41–44]. The low-rank approximation problem is first introduced with the rank function, that is,

$$\min_{\mathbf{X}} \quad rank(\mathbf{X}) \quad s.t. \ \ \mathbf{X} \in \mathcal{C},$$

where $rank(.)$ is the rank function, $\mathcal{C}$ is a convex set. Since the rank function is a difficult non-convex problem and hard to solve, the problem is generally relaxed by minimizing the nuclear norm of the estimated matrix, which is called as nuclear norm minimization (NNM) [45]. The nuclear norm of $\mathbf{X}$ is defined as

$$\|\mathbf{X}\|_* = \sum_i \sigma_i(\mathbf{X}),$$

where $\sigma_i(\mathbf{X})$ represents the ith singular value of $\mathbf{X}$. Due to the closed-form solution of the NNM approach, it has attracted significant attention and applications. However, for the NNM, all singular values are treated equally, which is not flexible enough to catch the homogenous region and texture information simultaneously. To improve the flexibility of NNM, a reweighted nuclear norm has been introduced and the reweighted norm of $\mathbf{X}$ is

$$\|\mathbf{X}\|_{w,*} = \sum_i w_i \sigma_i(\mathbf{X}),$$

where w_i are nonnegative weighting coefficients, ϵ is a small constant added to avoid singularities. This strategy is widely used for many practical problems (see [46–49]).

As the neighboring pixels tend to be homogeneous and constituted from the same endmembers, the low rankness of abundances is exploited frequently for hyperspectral unmixing [46,48, 50,51]. Considering that the highly correlated spectral signatures are also reflected as a high correlation among the pixel members of a local region, we estimate each abundance map with a low-rank constraint. To effectively impose the low-rank constraint without missing details, we introduce a reweighted nuclear norm to estimate the low-rankness of abundance maps [52]. Applying the reweighted nuclear norm for the rth abundance map $\mathbf{E}_r$, we get

$$\|\mathbf{E}_r\|_{\mathbf{w}_r,*} = \sum_i w_{r,i} \sigma_{r,i}(\mathbf{E}_r),$$

where $w_{r,i}$ are nonnegative weighting coefficients, and $\sigma_{r,i}(\mathbf{E}_r)$ denotes the ith singular value of $\mathbf{E}_r$. With the weighting vector, the weighted nuclear norm treats the individual singular values differently and promotes the sparsity on the singular values [51,53].

3.3. Model and algorithm

Based on NTF, we formulate our model by adding the endmember independence constraint and the low-rank approximation. Thus, the proposed model becomes

$$\begin{aligned}\min_{\mathbf{E},\mathbf{C}} \quad & \frac{1}{2}\|\mathcal{Y}-\sum_{r=1}^{R}\mathbf{E}_r\circ\mathbf{c}_r\|_F^2+\frac{\delta}{2}\|1_{I\times J}-\mathbf{E}\mathbf{D}^T\|_F^2 \\ & +\frac{\lambda_1}{2}\|\mathbf{C}.*\mathbf{W}\|_F^2+\lambda_2\sum_{r=1}^{R}\|\mathbf{E}_r\|_{w_r,*} \\ & s.t.\ \ \mathbf{E}\geq\mathbf{0},\mathbf{C}\geq\mathbf{0},\end{aligned} \tag{5}$$

where $\mathbf{E}=[\mathbf{E}_1,\ldots,\mathbf{E}_R]$, $\mathbf{C}=[\mathbf{c}_1,\ldots,\mathbf{c}_R]$, $\mathbf{D}=[\mathbf{D}_1,\ldots,\mathbf{D}_R]$, $\mathbf{D}_i\in\mathbb{R}^{J\times J}$, $(i=1,2,\ldots,R)$, is an identity matrix.

We now solve (5) by the augmented multiplicative algorithm, similarly as in [54]. We introduce an auxiliary variable $\mathbf{U}$ for $\mathbf{E}$, so the objective function is modified as

$$\begin{aligned}\min_{\mathbf{E},\mathbf{C},\mathbf{U}} \quad & \frac{1}{2}\|\mathcal{Y}-\sum_{r=1}^{R}\mathbf{E}_r\circ\mathbf{c}_r\|_F^2+\frac{\delta}{2}\|1_{I\times J}-\mathbf{E}\mathbf{D}^T\|_F^2 \\ & +\frac{\lambda_1}{2}\|\mathbf{C}\cdot*\mathbf{W}\|_F^2+\lambda_2\sum_{r=1}^{R}\|\mathbf{U}_r\|_{w_r,*} \\ & s.t.\ \ \mathbf{E}\geq\mathbf{0},\mathbf{C}\geq\mathbf{0},\mathbf{E}_r=\mathbf{U}_r.\end{aligned} \tag{6}$$

Substituting constraints into the problem (6), we obtain the Lagrange function

$$\begin{aligned}\mathcal{L}(\mathbf{E},\mathbf{C},\mathbf{U})=&\frac{1}{2}\|\mathcal{Y}-\sum_{r=1}^{R}\mathbf{E}_r\circ\mathbf{c}_r\|_F^2+\frac{\delta}{2}\|1_{I\times J}-\mathbf{E}\mathbf{D}^T\|_F^2 \\ &+\frac{\lambda_1}{2}\|\mathbf{C}\cdot*\mathbf{W}\|_F^2+\lambda_2\sum_{r=1}^{R}\|\mathbf{U}_r\|_{w_r,*}+\frac{\mu}{2}\|\mathbf{E}-\mathbf{U}\|_F^2 \\ &+\mathrm{Tr}(\Gamma\mathbf{E})+\mathrm{Tr}(\Phi\mathbf{C}),\end{aligned} \tag{7}$$

where Γ and Φ are Lagrange multipliers for each nonnegative variable in (6), and $\mu>0$ is a penalty parameter.

For the **E**-subproblem, removing the terms that are not related to **E** in (7), we slove the following minimization problem

$$\min_{\mathbf{E}}\frac{1}{2}\|\mathbf{Y}_{(1)}-\mathbf{M}_1\mathbf{E}^T\|_F^2+\frac{\delta}{2}\|1_{I\times J}-\mathbf{E}\mathbf{D}^T\|_F^2+\frac{\mu}{2}\|\mathbf{E}-\mathbf{U}\|_F^2, \tag{8}$$

where $\mathbf{M}_1=\mathbf{D}\bar{\odot}\mathbf{C}$. Considering the convexity of the problem (8) and the Karush-Kuhn–Tucker (KKT) conditions, when the problem (8) reaches its optimal value, we have

$$\begin{aligned}&\mathbf{Y}_{(1)}^T\mathbf{M}_1-\mathbf{E}\mathbf{M}_1^T\mathbf{M}_1+\delta(\mathbf{1}_{I\times J}-\mathbf{E}\mathbf{D}^T)\mathbf{D}+\mu(\mathbf{E}-\mathbf{U})-\Gamma=\mathbf{0},\\ &\Gamma.*\mathbf{E}=\mathbf{0}.\end{aligned} \tag{9}$$

According to (9), the update rule for **E** is obtained

$$\begin{aligned}\mathbf{E}^{(t+1)}=&\mathbf{E}^{(t)}.*(\mathbf{Y}_{(1)}^T\mathbf{M}_1+\delta\mathbf{1}_{I\times J}\mathbf{D}+\mu\mathbf{U})\\ &./(\delta\mathbf{E}^{(t)}\mathbf{D}^T\mathbf{D}+\mathbf{E}^{(t)}\mathbf{M}_1^T\mathbf{M}_1+\mu\mathbf{E}^{(t)}).\end{aligned} \tag{10}$$

For the **C**-subproblem, we get

$$\mathbf{C}^{(t+1)}=\arg\min_{\mathbf{C}}\frac{1}{2}\|\mathbf{Y}_{(3)}-\mathbf{M}_2\mathbf{C}^T\|_F^2+\frac{\lambda_1}{2}\|\mathbf{C}.*\mathbf{W}\|_F^2+\mathrm{Tr}(\Phi\mathbf{C}), \tag{11}$$

where $\mathbf{M}_2=[(\mathbf{E}_1\bigodot\mathbf{D}_1)\mathbf{1}_L\cdots(\mathbf{E}_R\bigodot\mathbf{D}_R)\mathbf{1}_L]$. Similarly in the **E**-subproblem, the solution of the **C**-subproblem is

$$\mathbf{C}^{(t+1)}=\mathbf{C}^{(t)}.*(\mathbf{Y}_{(3)}^T\mathbf{M}_2)./(\mathbf{C}^{(t)}\mathbf{M}_2^T\mathbf{M}_2+\lambda_1\mathbf{C}^{(t)}\mathbf{W}^{(t)}). \tag{12}$$

And $\mathbf{W}^{(t)}=[\mathbf{w}_1^{(t)},\ldots,\mathbf{w}_R^{(t)}]$, $\mathbf{w}_i^{(t)}$ is the ith column in $\mathbf{W}^{(t)}$ and updated by

$$\mathbf{w}_i^{(t)}=1./(\mathrm{BF}(\mathbf{c}_i^{(t-1)})+\eta), \tag{13}$$

where η is small value, $\mathbf{c}_i^{(t-1)}$ is the ith column in $\mathbf{C}^{(t-1)}$, and ./ denotes element-wise division.

Due to the existence of the low-rank constraint on $\mathbf{U}_r$, we divide **U** into R submatrices, where each one is with the same size as $\mathbf{E}_r$. Recall that $\|\mathbf{E}-\mathbf{U}\|_F^2=\sum_{r=1}^{R}\|\mathbf{E}_r-\mathbf{U}_r\|_F^2$, the **U**-subproblem is transformed to R subproblems, each of which is

$$\mathbf{U}_r^{(t+1)}=\arg\min_{\mathbf{U}_r}\ \frac{\mu}{2}\|\mathbf{E}_r-\mathbf{U}_r\|_F^2+\lambda_2\|\mathbf{U}_r\|_{w_r,*}. \tag{14}$$

Before solving $\mathbf{U}_r$ subproblems, we introduce some definitions. Given a matrix $\mathbf{X}$, $rank(\mathbf{X})=j$, the singular value decomposition (SVD) of $\mathbf{X}$ is

$$\mathrm{SVD}(\mathbf{X})=\tilde{\mathbf{P}}Diag(\delta_1,\ldots,\delta_j)\tilde{\mathbf{Q}}.$$

where $\delta=(\delta_1,\ldots,\delta_j)$ denotes singular values of $\mathbf{X}$. The singular value shrinkage operator $shr(.,\tau)$ on $\mathbf{X}$ is defined as

$$shr(\mathbf{X},\tau)=\tilde{\mathbf{P}}Diag(max\{\delta-\tau,\mathbf{0}\})\tilde{\mathbf{Q}}. \tag{15}$$

Then, the solution of Eq. (14) is denoted as

$$\mathbf{U}_r^{(t+1)}=shr(\mathbf{E}_r^{(t+1)}-\mathbf{U}_r^{(t)},\frac{\lambda_2}{\mu}w_r), \tag{16}$$

where w_r is the weighting vector, its ith entry $w_{r,i}=\frac{1}{\delta_{r,i}+\epsilon}$, $i=1,\ldots,v$, $\delta_{r,i}$ is the ith singular value of $\mathbf{E}_r^{(t+1)}-\mathbf{U}_r^{(t)}$. According to the above analysis, we summarize the corresponding algorithm to solve EIC-NTF in Algorithm 1. Here, we briefly present the computational complexity analysis of Algorithm 1. According to Algorithm 1, each iteration mainly contains three updating steps in the following.

(1) According to the update rule of **E** in (10), the number of multiplication operations is $RJ(5I+IJL+3IJ+JLRL+IJLRJ)$.
(2) According to the update rule of **C** in (12), the number of multiplication operations is $RL(4+IJ+IJR)$.
(3) According to the update rule of **U** in (16), the number of multiplication operations is $(IRJ)^2$.

Therefore, at each iteration, the computational complexity of EIC-NTF is $\mathbf{O}(IJ^2R^2L+ILR^2J^3+IJLR^2+I^2R^2J^2)$.

According to theoretic results from [55], a limit point of the sequence $\{\mathbf{E}^{(t)},\mathbf{U}^{(t)},\mathbf{U}^{(t)}\}$ is a local minima, then the limit point must meets the KKT conditions. However, as said in [56,57], it is not clear if the limit point obtained by the multiplicative iterative algorithm satisfies the KKT conditions. In addition, due to the non-convexity of EIC-NTF and the use of the reweighting matrix **W** in the update rule of **C**, it is hard to guarantee that the Lagrange function $\mathcal{L}$ is convergent. Nevertheless, it is worth mentioning that, despite the convergence is not theoretically guaranteed, EIC-NTF exhibits a stable convergence behavior in our experiments in Section 4.4.

Algorithm 1: EIC-NTF.

Input: An HSI cube $\mathcal{Y}\in\mathbb{R}^{I\times J\times L}$;
The parameters δ, λ_1, λ_2 and μ.
The number of endmembers R.
Initialization: $\mathbf{E}^{(0)},\mathbf{C}^{(0)},\mathbf{W}^{(0)},\mathbf{U}_r^{(0)}=\mathbf{E}_r^{(0)}$ for $r=1,\ldots,R$.
Repeat:
Update $\mathbf{E}^{(t+1)}$ by (10)
Update $\mathbf{C}^{(t+1)}$ by (12)
Update $\mathbf{W}^{(t+1)}$ by (13)
Update $\mathbf{U}_r^{(t+1)}$ by (16)
Until termination condition is met.

4. Synthetic data experiments

In this section, several synthetic and real-world experiments are conducted to illustrate the unmixing performance of our proposed method. Besides, we compare EIC-NTF with some state-of-the-art unmixing algorithms, NMF [19], $L_{1/2}$-NMF [22], TV-RSNMF [27], MCSNMF [29], MV-NTF [34], and MV-NTF-TV [35]. All tests are implemented on the platform of Windows 10 and MATLAB (R2019a) with an Intel Core i9-9900K, 3.60 GHz, and 32 GB RAM.

4.1. Experimental settings

Performance Measurement: To measure the unmixing performance, we choose spectral angle distance (SAD) and root mean square error (RMSE) as indices. The SAD evaluates the dissimilarity of the rth endmember signature $\hat{\mathbf{c}}_r$ and its estimated signature $\mathbf{c}_r$, which is defined as

$$\mathrm{SAD}_r = \arccos\left(\frac{\mathbf{c}_r^T\hat{\mathbf{c}}_r}{\|\mathbf{c}_r\|_2\|\hat{\mathbf{c}}_r\|_2}\right).$$

The RMSE measures the error between the real abundance map $\hat{\mathbf{E}}_r$ of rth endmember and its estimated map $\mathbf{E}_r$, which is defined as

$$\mathrm{RMSE}_r = \left(\frac{1}{N}\|\mathbf{E}_r - \hat{\mathbf{E}}_r\|_F^2\right)^{\frac{1}{2}},$$

where $N = I \times J$ is the number of pixels in the HSI. Generally, a lower value of SAD and RMSE denote a better unmixing performance [34].

Data Generation: The generation of synthetic data includes two steps: endmember selection and abundance generation. To demonstrate the unmixing performance of EIC-NTF, we select the following two data cubes.

DC1: For the simulated data cube 1 (DC1), we choose six pure endmembers (Carnallite, Ammonio-jarosite, Almandine, Brucite, Axinite, and Chlonte) from the USGS library as spectral matrix $\mathbf{C}$ [38], which has been shown in Fig. 2. For abundance generation, we adopt a modified strategy in [35], which contains the following steps

1. Generate an HSI, whose size is $z^2 \times z^2$, and it is composed of R endmembers. And divide it into z^2 blocks. Each of these blocks contains $z \times z$ pixels.
2. Given a mixing level θ, we select two endmembers from above six endmembers randomly to fill each pixel in a region and set the corresponding fractions be θ and $1-\theta$, respectively.
3. The image is processed using a $(2z+1) \times (2z+1)$ mean filter to generate mixed pixels.
4. We reset the proportions of all endmember in each pixel so that the abundance of each pixel satisfies the ASC constraint.

Rearrange the generated abundance, we get $\mathbf{E}$. With these steps, a clean HSI will be obtained according to LMM. Finally, the scene is contaminated by adding zero-mean white Gaussian noise with the signal to noise ratio (SNR) defined as follows

$$\mathrm{SNR} = 10\log_{10}\frac{\|\mathbf{Y}\|_F^2}{\|\boldsymbol{\alpha}\|_F^2},$$

where $\mathbf{Y}$ represents a synthetic HSI data with some endmembers and α is added with white noise.

DC2: For the simulated data cube 2 (DC2), we adopt a synthetic data cube with a size of 128×128, which has been widely used in many unmixing methods [58,59]. This data cube contains five endmembers with 431 bands, the corresponding true fractional abundances for each of the five endmembers are shown in Fig. 10. In Fig. 9(a), we show the 90th band of DC2.

Initialization: In the following experiments, random initialization is utilized to initialize $\mathbf{E}$ and $\mathbf{C}$. Specifically, $\mathbf{C}$ is initialized by setting their entries to random values in the interval [0, 1]. And we initialize $\mathbf{E}$ using the strategy similar to the generation of abundance. The initialization of other comparing algorithms is the same as our initialization.

4.2. Experiments on DC1

Parameter Analysis: In the proposed model, there are four parameters: δ, λ_1, λ_2, and μ. As both λ_2 and μ control the strictness of the low-rank constraint, we only analyze the influence of δ, λ_1, and μ. To select the optimal parameters, we generate DC1 with $z = 8$, $R = 6$, $\beta = 0.8$, and SNR = 30 dB to conduct the following experiments.

(1) The Influence of δ: Setting $\lambda_1 = 2$, $\lambda_2 = 1$, and $\mu = 0.001$, we test SADs and RMSEs when δ is selected from {0.1, 0.5, 1, 2, 3, 4}. Fig. 4(a) shows the performance of our method to δ in terms of SAD and RMSE. According to Fig. 4(a), both SAD and RMSE are stable when $\delta = 2, 3, 4$, which are the best results. Therefore, we fix $\delta = 3$ in the following experiments.

(2) The Influence of λ_1: Recall that parameter λ_1 controls the contribution of endmember independence constraint. Here, Fig. 4(b) shows SADs and RMSEs when λ_1 is selected from {0.1, 0.5, 1, 2, 3, 4} with $\delta = 2, \lambda_2 = 1$, and $\mu = 0.001$, According to Fig. 4(b), when $\lambda_1 = 2, 3, 4$, both SAD and RMSE are the best results. Therefore, we fix $\lambda_1 = 3$ in the following experiments.

(3) The Influence of μ: In Eq. (7), $\mu > 0$ is a penalty parameter, which has an influence on the low-rank approximation. Fig. 4(c) shows SADs and RMSEs when μ is selected from {0.001, 0.01, 0.1, 1, 5} with $\delta = 2$, $\lambda_1 = 3$, and $\lambda_2 = 1$. According to Fig. 4(c), when $\mu = 0.1$, both SAD and RMSE are the best results. Therefore, we fix $\mu = 0.1$ in the following experiments.

Conclusively, in the following experiments, we set $\delta = 3$, $\lambda_1 = 3$, and $\mu = 0.1$.

(4) The Influence of the Endmember Independence Constraint: To illustrate the effectiveness of the endmember independence constraint, we measure the unmixing performance of EIC-NTF under different values of λ_1 on DC2. In Fig. 5, we present the estimated endmembers obtained by EIC-NTF and EIC-NTF with $\lambda_1 = 0$ on DC2. From Fig. 5, EIC-NTF provides more similar estimated endmembers to the references than EIC-NTF with $\lambda_1 = 0$ for endmembers 1 to 5.

Performance in different cases: In this part, we compare the seven methods in different cases on DC1.

(1) Performance under different noise levels: This experiment aims to measure the unmixing performance under different noise levels for seven different algorithms. The DC1 is generated with $z = 8$, $R = 6$, and $\theta = 0.8$, then corrupted by noise with SNR = {20 dB, 25 dB, 30 dB, 35 dB, 40 dB}. Fig. 6(a) presents all algorithms' unmixing performance in terms of SAD and RMSE under different noise levels. According to Fig. 6(a), with the noise level increase, the values of SAD for these seven methods increase. Unmixing performances of NMF-based methods are more stable in terms of SAD. MCSNMF obtains better RMSEs than MV-NTF under different noise levels. The proposed method obtains the best SAD and RMSE for all noise levels.

(2) Performance under Different Mixing Levels: In this experiment, we discuss the unmixing performance of seven methods under different mixing levels. The mixing level depends on the parameter θ, i.e., a larger θ implies a smaller mixing level. Select θ from the set {0.5, 0.6, 0.7, 0.8, 0.9}, we generate the DC1 with $z = 8$, $R = 6$, and SNR = 30 dB. In Fig. 6(b), we show SADs

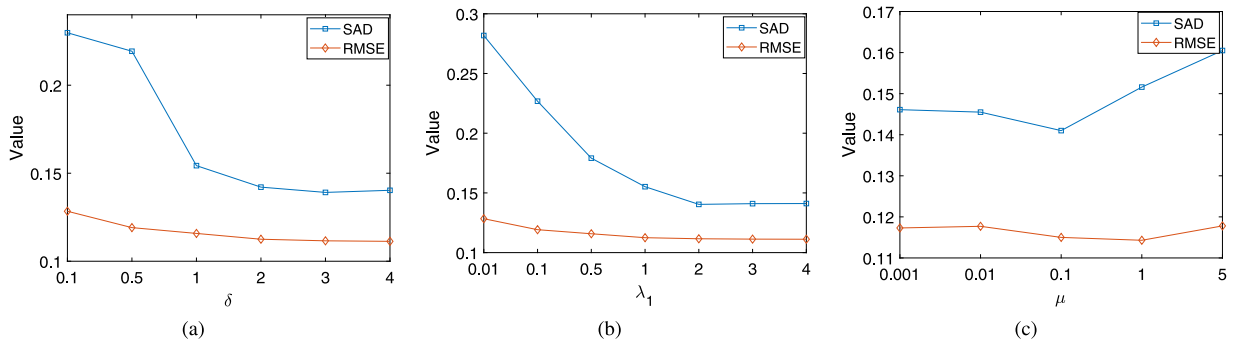

Fig. 4. Performance of EIC-NTF on DC1 in terms of SAD and RMSE with respect to different parameters. (a) δ. (b) λ_1. (c) μ.

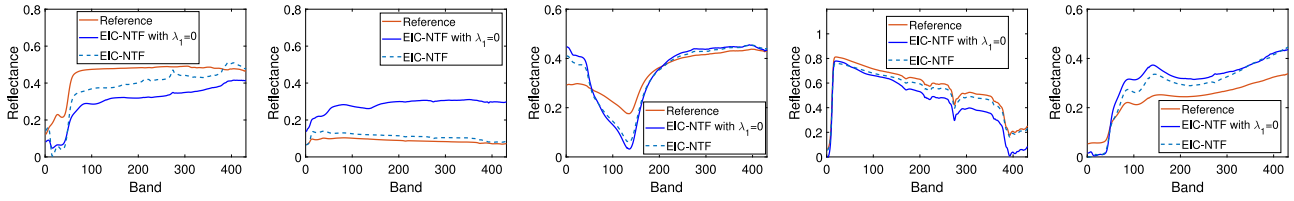

Fig. 5. References and estimated endmember curves by EIC-NTF with different values of λ_1 for DC2. From left to right: endmembers 1 to 5.

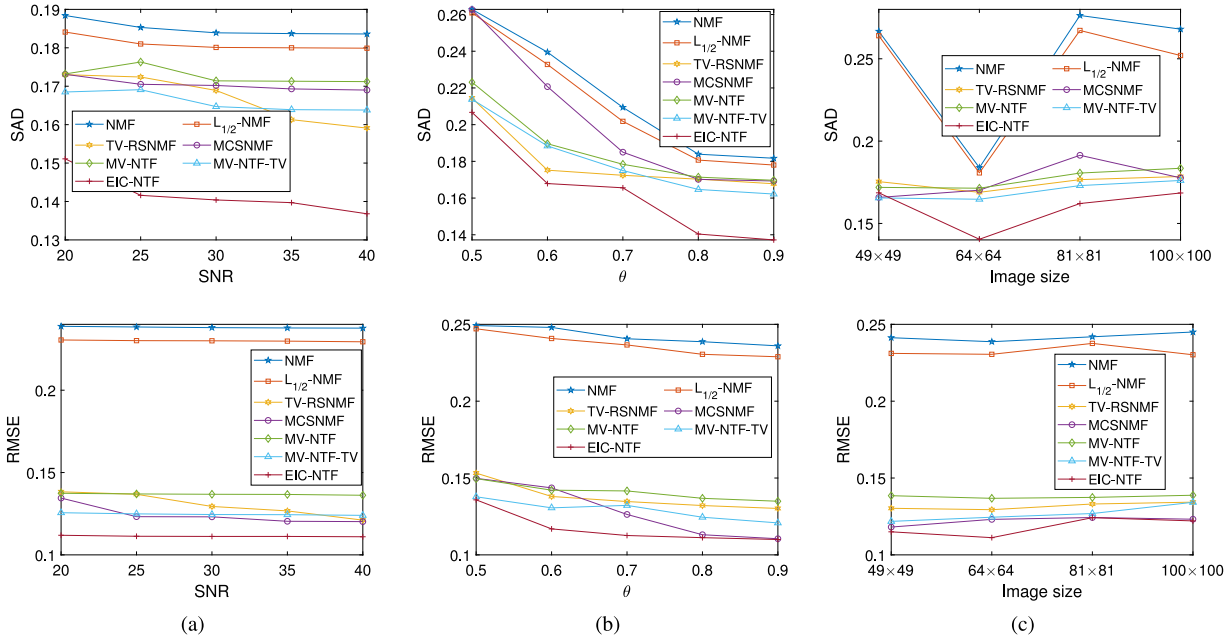

Fig. 6. Comparison of different unmixing methods with respect to different cases.

Table 1
Means and deviations of SAD and RMSE of different algorithms on DC2.

	NMF	$L_{1/2}$-NMF	TV-RSNMF	MCSNMF	MV-NTF	MV-NTF-TV	EIC-NTF
End 1	0.3624±5.62%	0.3522±5.56%	0.2629±5.28%	0.2270±5.36%	0.2224±4.35%	0.2194±4.22%	**0.1007±4.95%**
End 2	0.2937±6.28%	0.2858±5.89%	0.0634±7.17%	0.0608±6.98%	0.11136±4.81%	0.1356±4.95%	**0.0576±6.64%**
End 3	0.2092±4.42%	0.2123±4.52%	0.1933±8.26%	0.1854±7.63%	0.1259±6.41%	0.1175±6.55%	**0.1034±3.75%**
End 4	0.1890±6.19%	0.1792±6.32%	0.0343±1.44%	0.1810±2.35%	0.1372±0.93%	0.1191±1.30%	**0.0081±0.79%**
End 5	0.1010±6.44%	**0.0961±6.31%**	0.1515±3.39%	0.1325±2.58%	0.1794±7.11%	0.1741±8.58%	0.1494±1.38%
Mean	0.2310±3.28%	0.2259±3.26%	0.1261±3.55%	0.1916±3.64%	0.1557±2.47%	0.1511±2.56%	**0.0838±2.12%**
RMSE	0.2002±3.39%	0.2004±3.15%	0.1763±2.01%	0.2493±2.12%	0.1763±2.14%	0.1701±2.16%	**0.1346±2.01%**

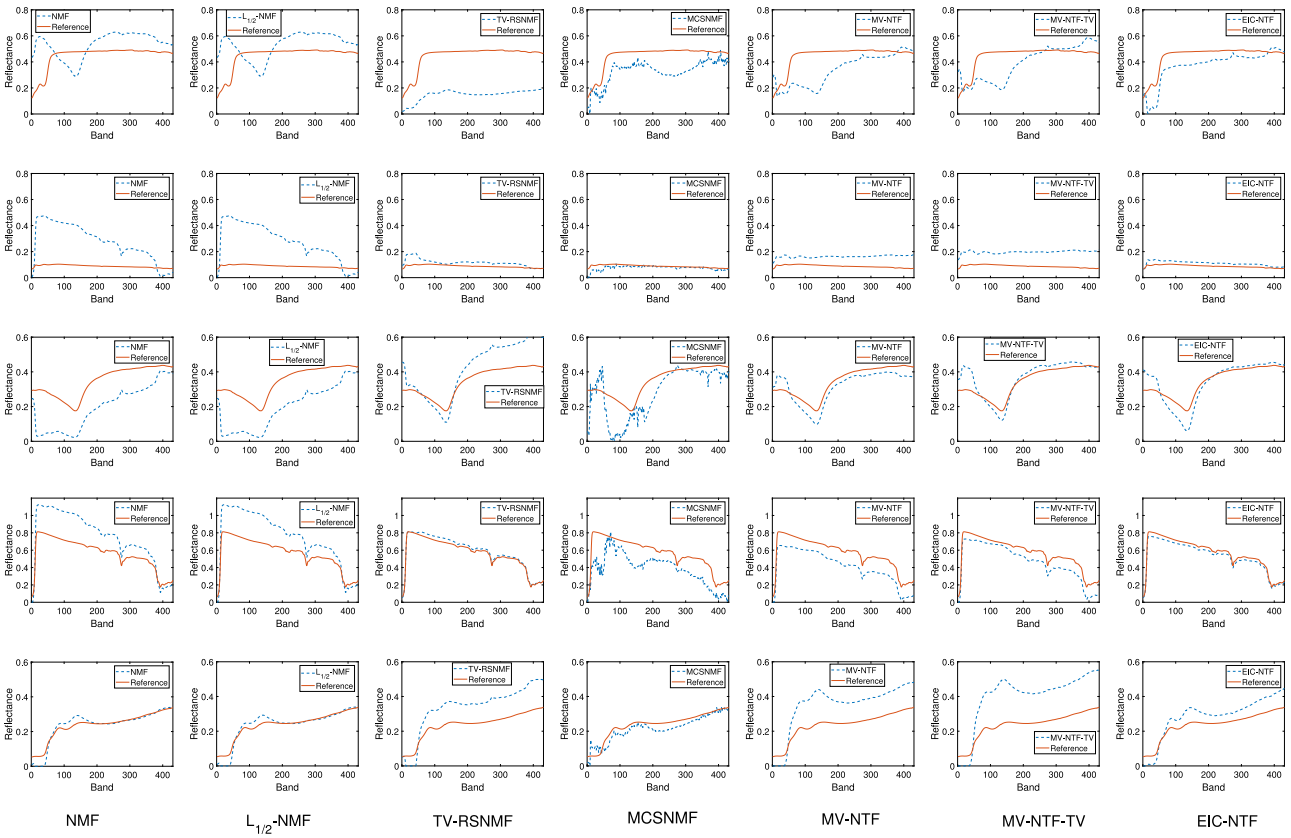

Fig. 7. References and estimated spectral curves by different unmixing algorithms on DC2. From left to right: endmembers 1 to 5.

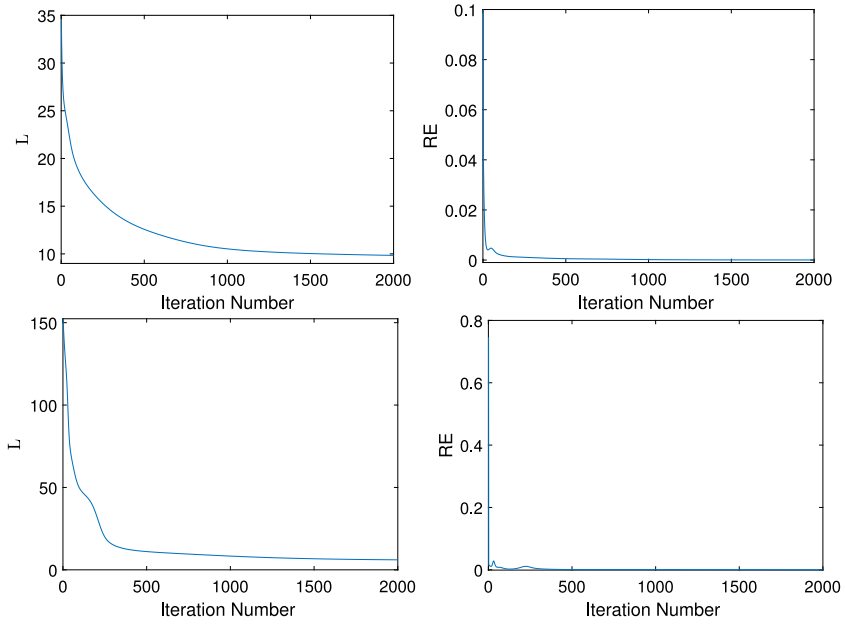

Fig. 8. Convergence curves of EIC-NTF for (top row) DC1 and (bottom row) DC2 .

and RMSEs for seven methods under different mixing levels. From Fig. 6(b), the higher the mixing levels are, the worse the unmixing results for these comparing methods are. In terms of SAD and RMSE, the proposed method is better than others under different mixing levels.

(3) Performance under different image sizes: This experiment is to measure seven methods under different image sizes. We choose the image size from $\{49\times 49, 64\times 64, 81\times 81, 100\times 100\}$, set $R = 6, \theta = 0.8$, and SNR $=$ 30 dB to generate the DC1. SADs and RMSEs for comparing methods with different image sizes are shown in Fig. 6(c). From Fig. 6(c), seven methods behave worst when the size is 81×81 and behave best when the size is 64×64 in terms of SAD. NMF and $L_{1/2}$-NMF obtain similar results to SAD and RMSE. Under different image sizes, EIC-NTF outperforms the other six approaches.

Table 2
Means and standard deviations of SAD on Jasper Ridge data and Urban data.

Jasper Ridge data

Algorithm	NMF	$L_{1/2}$-NMF	TV-RSNMF	MCSNMF	MV-NTF	MV-NTF-TV	EIC-NTF
Tree	0.2230±3.13%	0.2405±2.39%	0.2461±3.43%	**0.2080±2.39%**	0.2231±1.31%	0.2232±2.61%	0.2109±2.30%
Water	0.2273±3.32%	0.2329±2.71%	**0.1380±1.23%**	0.3668±1.23%	0.1743±4.83%	0.1743±2.78%	0.1411±1.84%
Soil	0.3073±3.36%	0.3064±3.21%	0.2300±4.72%	**0.1177±4.72%**	0.1794±5.15%	0.1799±4.82%	0.1891±3.24%
Road	0.2040±1.82%	0.1959±2.41%	0.1961±3.12%	0.1556±3.12%	0.1907±1.23%	0.1910±2.74%	**0.1370±2.79%**
Mean	0.2423±3.51%	0.2439±3.31%	0.2070±2.56%	0.2170±2.56%	0.1918±1.27%	0.1921±2.64%	**0.1695±4.40%**

Urban data

Algorithm	NMF	$L_{1/2}$-NMF	TV-RSNMF	MCSNMF	MV-NTF	MV-NTF-TV	EIC-NTF
Tree	0.1246±3.45%	0.1167±3.31%	0.1804±2.65%	0.1694±2.96%	0.1286±4.34%	0.1252±3.12%	**0.0643±2.91%**
Grass	0.2405±3.80%	0.2172±2.65%	0.1205±4.12%	0.1205±2.20%	0.1322±3.59%	0.1314±3.15%	**0.1177±1.52%**
Roof	0.4148±2.47%	0.4089±1.98%	0.3795±3.66%	0.3559±1.19%	0.3180±3.77%	0.3151±2.44%	**0.3038±1.18%**
Asphlt	0.3461±3.82%	0.3332±2.36%	0.1179±2.73%	**0.1172±1.38%**	0.2676±3.67%	0.2407±5.68%	0.1930±3.89%
Mean	0.2815±2.71%	0.2744±2.31%	0.1987±1.95%	0.1907±1.71%	0.2120±3.95%	0.2018±5.82%	**0.1797±1.37%**

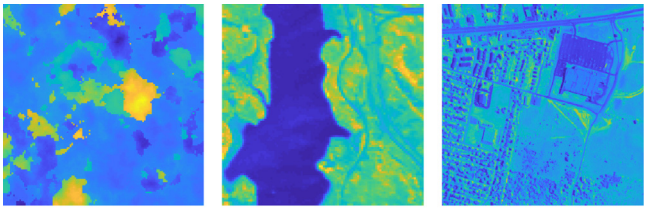

(a) (b) (c)

Fig. 9. The false-color images for DC2, Jasper Ridge data, and Urban data. Particularly, the bands of 90, 50, 90 are selected.

4.3. Experiments on DC2

We now study the performance of EIC-NTF and the compared algorithms on DC2. We adopt 20 trials for each method and show the means and deviations of SAD and RMSE of different algorithms in Table 1. From Table 1, EIC-NTF obtains the lowest SAD for the endmembers 1 to 4, $L_{1/2}$-NMF achieves the best SAD with respect to the endmember 5. In conclusion, EIC-NTF obtains the best mean SAD and the lowest RMSE.

To see unmixing performance visibly, we show the estimated endmember signatures in Fig. 7 and the corresponding abundance maps in Fig. 10. According to Fig. 7, the spectral curves for the endmember 5 estimated by NMF-based methods are closer to the reference than other methods. The spectral curves for the endmembers 1 to 4 estimated by EIC-NTF are closer to the references, which is consistent with the results in Table 1. From Fig. 10, NMF-based methods recover the most outline of the abundances, MV-NTF and MV-NTF-TV fail to separate the abundance maps corresponding to the endmembers 1 to 3. For the estimated abundance maps corresponding to the endmember 1, the comparing six methods do not retrieve the information, while EIC-NTF recovers the most information of the abundance map. In addition, EIC-NTF estimates most information of all abundance maps corresponding to the five endmembers.

4.4. Convergence analysis

The goal of this experiment is to numerically analyze the convergence of EIC-NTF. To this end, Fig. 8 plots the curves of the relative error (RE) and the Lagrange function value versus the iteration number on DC1 with the size of 64 × 64, SNR = 30 dB, and $\theta = 0.8$ and DC2. The RE is defined as follows:

$$\mathrm{RE} = \frac{|\mathcal{L}(E^{(t)}, C^{(t)}, U^{(t)}) - \mathcal{L}(E^{(t+1)}, C^{(t+1)}, U^{(t+1)})|}{\mathcal{L}(E^{(t)}, C^{(t)}, U^{(t)})}.$$

From Fig. 8, the convergence curves of EIC-NTF tend to be stable practically.

5. Real-world data experiments

In this section, we conduct Real-World Data Experiments on Jasper Ridge data set and Urban data set to evaluate the performance of the proposed method. These two data sets are utilized widely [60,61]. The initialization strategy and parameter settings are the same as the synthetic data experiments.

5.1. Jasper Ridge Data Set

Jasper Ridge Data Set contains 512 × 614 pixels with 224 bands, and each band covers wavelength ranging from 0.38 to 2.5 μm. This data is generated by the Airborne Visible/Infrared Imaging Spectrometer (AVIRIS) over the Jasper Ridge in central California, USA [62]. Since it is difficult to get the ground truth for the HSI, we consider a 100 × 100-pixel sub-image. Due to dense water vapor and atmospheric effects, we remove the channels 1-3, 108-112, 154-166, and 220-224 and remain 198 channels. We set this data include four endmembers: road, soil, water, and tree. In Fig. 9(b), we show the 50th band of Jasper Ridge data set.

In Table 2, the SAD results of the seven unmixing methods are presented. From Table 2, we see that EIC-NTF achieves the best SAD for the endmember road. MCSNMF estimates the endmembers tree and soil better, but fails to the endmember water. Furthermore, Figs. 11 and 12 show the endmember signatures and the corresponding abundance maps estimated by the seven methods. By Fig. 11, the spectral curves for the endmembers soil and tree estimated by MCSNMF are closer to the references. For the endmember road, the result obtained by EIC-NTF is closer to reference. According to Fig. 12, even abundance maps estimated by NMF and $L_{1/2}$-NMF remain most information in terms of the endmembers soil and tree, there exist some regions that correspond to the other endmembers. MV-NTF and MV-NTF-TV achieve the outline of each abundance map, but miss some details

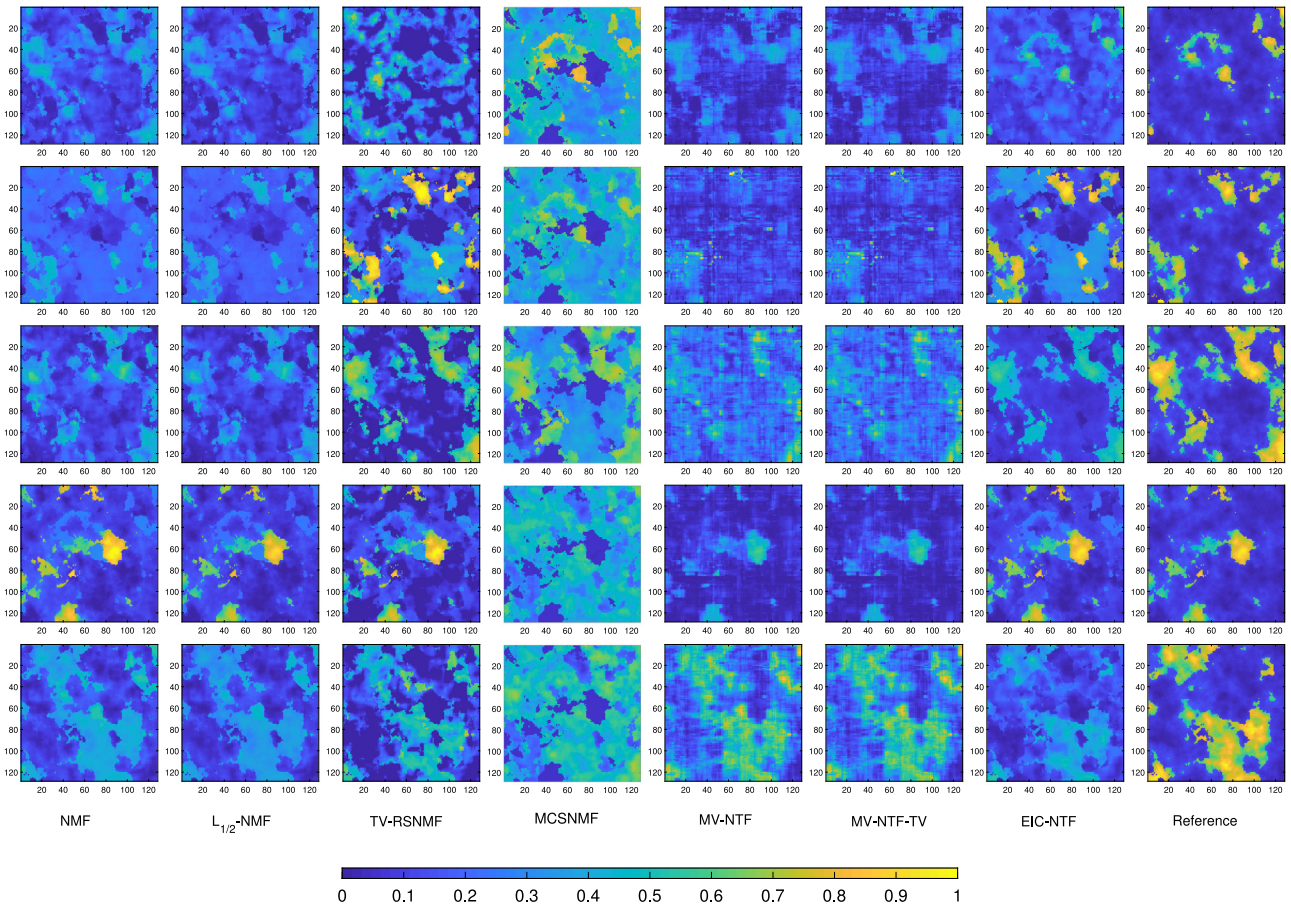

Fig. 10. References and estimated abundance maps by different unmixing algorithms on DC2 for endmembers 1 to 5.

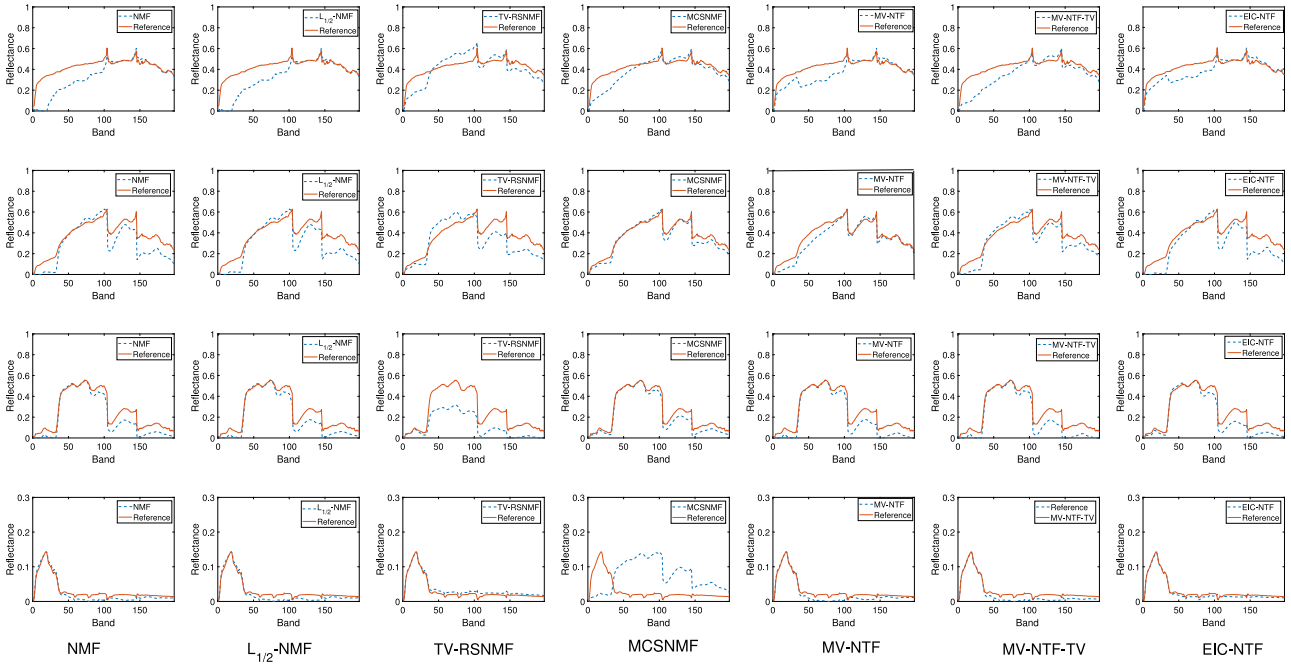

Fig. 11. References and estimated spectral curves by different unmixing algorithms for road, soil, tree, and water on Jasper Ridge data set.

for the endmembers road and soil. EIC-NTF achieves competitive unmixing performance compared with the other six unmixing approaches on this data set, especially for the endmembers road and water.

5.2. HYDICE Urban Data Set

Urban data set is one of the most widely used hyperspectral data used in the hyperspectral unmixing study, which is collected

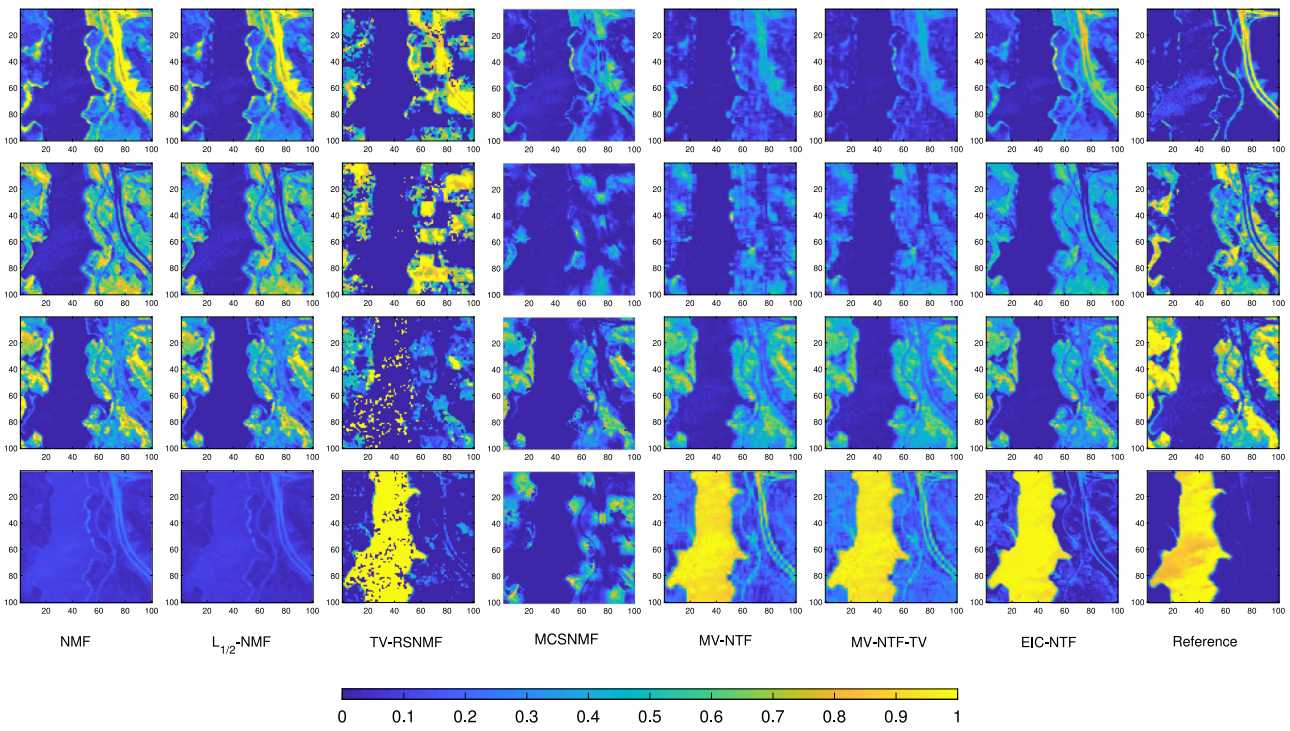

Fig. 12. References and estimated abundance maps by different unmixing algorithms for road, soil, tree, and water on Jasper Ridge data.

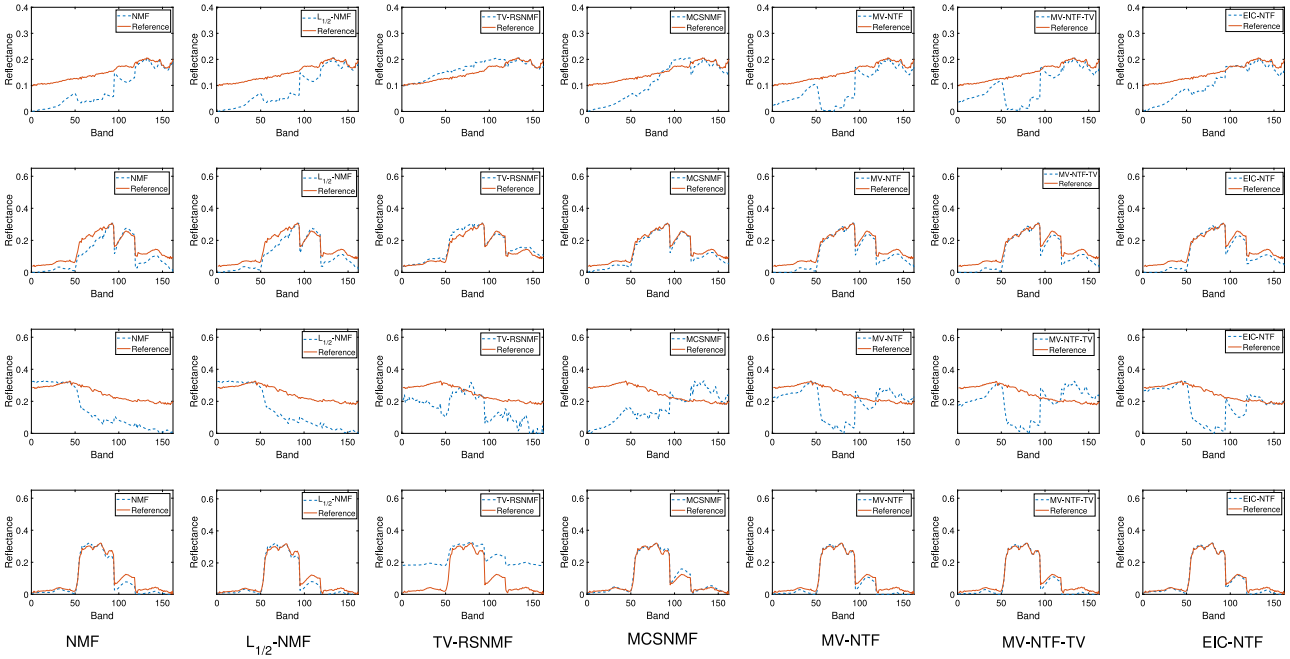

Fig. 13. References and estimated spectral curves by different unmixing algorithms for asphalt, grass, roof, and tree on Urban data.

by the Hyperspectral Digital Imagery Collection Experiment (HYDICE) in an urban area [63]. This image has 307 × 307 pixels and 210 bands, whose wavelength ranging from 0.4 to 2.5 μm. Due to dense water vapor and atmospheric effects), we remain 162 bands. In this experiment, we assume that Urban data is composed of 4 endmembers: asphalt, grass, roof, tree. In Fig. 9(c), we show the 90th band of Urban data set.

We show the SAD results tested by the comparing methods in Table 2. In Table 2, EIC-NTF achieves the best SAD for the endmembers tree, grass, and roof, MCSNMF obtains the best SAD for the endmember asphalt. In addition, Figs. 13 and 14 show the endmember signatures and the corresponding abundance maps estimated by seven methods, respectively. By Fig. 13, the spectral curves for the endmember tree estimated by NTF-based methods are closer to the references compared with the NMF-based methods. For MV-NTF and MV-NTF-TV, the estimated endmember signatures of asphalt and roof are similar, which means the incomplete separation of the mixed pixels. EIC-NTF method with the endmember independence constraint avoids this problem, and the estimated endmembers signatures of asphalt and roof are more accurate. According to Fig. 14, abundance maps of roof

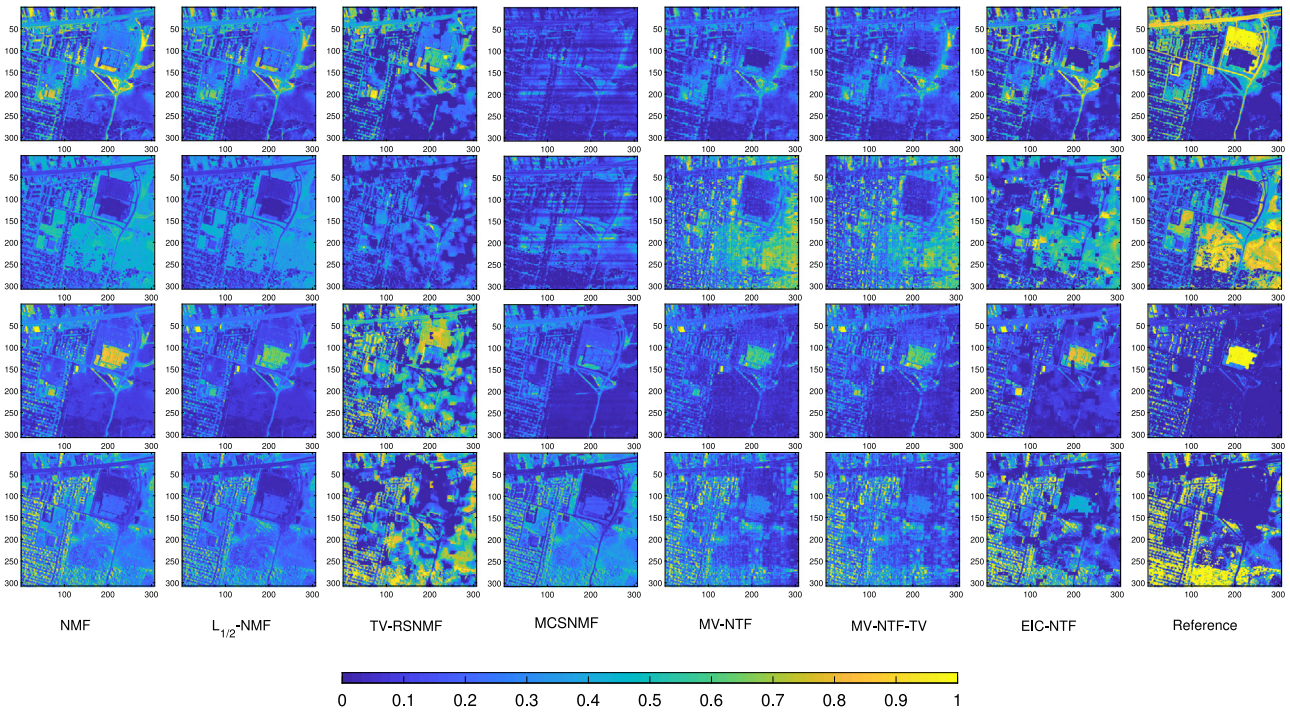

Fig. 14. References and estimated abundance maps by different unmixing algorithms for asphalt, grass, roof, and tree on Urban data.

obtained by NMF-based methods remain more details comparing with the MV-NTF-based methods, but include some regions belonging to other abundance maps. Abundance maps of grass and tree obtained by MV-NTF and MV-NTF-TV are closer to references comparing with the NMF-based methods. However, these methods generate some noise in each abundance map and miss some details. Compared with the above six unmixing approaches, abundance maps obtained by EIC-NTF are closer to references and smoother. In general, EIC-NTF obtains better unmixing results comparing with the other six methods.

6. Conclusion

In this paper, we propose an unmixing algorithm named endmember independence constrained hyperspectral unmixing via nonnegative tensor factorization (EIC-NTF). To alleviate the impact of highly correlated spectral signatures, EIC-NTF introduces an endmember independence constraint on endmembers and a low-rank constraint on each abundance map. EIC-NTF relieves the effect of the highly correlated spectral signatures from the aspect of endmembers and abundance maps with these two constraints. To solve the proposed model, an augmented multiplicative algorithm is proposed to obtain updated rules. Experimental results on both synthetic data and real-world data demonstrate the effectiveness of our algorithm. Especially, real-data experiments also show the advantages of our method in remaining details of abundance maps over the other two NTF-based approaches. However, our unmixing results exist some regions that are not actually presented in references in some cases. In the future, additional potential property from abundance maps and endmember signatures will be considered.

CRediT authorship contribution statement

Jin-Ju Wang: Methodology, Software, Writing - original draft. **Ding-Cheng Wang:** Writing - review & editing, Visualization preparation, Resources. **Ting-Zhu Huang:** Visualization preparation, Resources, Supervision. **Jie Huang:** Conceptualization, Writing - review & editing, Visualization preparation. **Xi-Le Zhao:** Writing - review & editing, Visualization preparation. **Liang-Jian Deng:** Writing - review & editing, Visualization preparation.

Declaration of competing interest

The authors declare that they have no known competing financial interests or personal relationships that could have appeared to influence the work reported in this paper.

Acknowledgment

The authors would like to thank the editors and the three anonymous reviewers for their constructive, detailed, and helpful advice regarding this paper.

This research is supported in part by NSFC, PR China (Grant No. 61772003, 61876203, 61702083), in part by Key Projects of Applied Basic Research in Sichuan Province, PR China (Grant No. 2020YJ0216), and in part by the Fundamental Research Funds for the Central Universities, PR China (Grant No. ZYGX2019J093).

References

[1] F. Melgani, L. Bruzzone, Classification of hyperspectral remote sensing images with support vector machines, IEEE Trans. Geosci. Remote Sens. 42 (8) (2004) 1778–1790.
[2] H. Zhang, J. Li, Y. Huang, L. Zhang, A nonlocal weighted joint sparse representation classification method for hyperspectral imagery, IEEE J. Sel. Topics Appl. Earth Observ. Remote Sens. 7 (6) (2014) 2056–2065.
[3] D.W.J. Stein, S.G. Beaven, L.E. Hoff, E.M. Winter, A.P. Schaum, A.D. Stocker, Anomaly detection from hyperspectral imagery, IEEE Signal Process. Mag. 19 (1) (2002) 58–69.
[4] L. Deng, M. Feng, X. Tai, The fusion of panchromatic and multispectral remote sensing images via tensor-based sparse modeling and hyper-Laplacian prior, Inf. Fusion 52 (2019) 76–89.
[5] B. Zhang, L. Zhuang, L. Gao, W. Luo, Q. Ran, Q. Du, PSO-EM: A hyperspectral unmixing algorithm based on normal compositional model, IEEE Trans. Geosci. Remote Sens. 52 (12) (2014) 7782–7792.
[6] J.M. Bioucasdias, A. Plaza, N. Dobigeon, M. Parente, Q. Du, P.D. Gader, J. Chanussot, Hyperspectral unmixing overview: Geometrical, statistical, and sparse regression-based approaches, IEEE J. Sel. Topics Appl. Earth Observat. Remote Sens. 5 (2) (2012) 354–379.

[7] G. Zhang, F. Fang, Y. Ying, Framelet-based sparse unmixing of hyperspectral images, IEEE Trans. Image. Process 25 (4) (2016) 1516–1529.
[8] Y. Xu, F. Fang, Z. Guixi, Similarity-guided and -regularized sparse unmixing of hyperspectral data, IEEE Geosci. Remote. Sens. Lett. 12 (2015) 1–5.
[9] M. Iordache, J.M. Bioucas-Dias, A. Plaza, Sparse unmixing of hyperspectral data, IEEE Trans. Geosci. Remote Sens. 49 (6) (2011) 2014–2039.
[10] X. Lu, H. Wu, Y. Yuan, P. Yan, X. Li, Manifold regularized sparse NMF for hyperspectral unmixing, IEEE Trans. Geosci. Remote Sens. 51 (5) (2013) 2815–2826.
[11] J. Wang, T. Huang, J. Huang, H. Dou, L. Deng, X. Zhao, Row-sparsity spectral unmixing via total variation, IEEE J. Sel. Topics Appl. Earth Observ. Remote Sens. 12 (12) (2019) 5009–5022.
[12] N. Keshava, J.F. Mustard, Spectral unmixing, IEEE Signal Process. Mag. 19 (1) (2002) 44–57.
[13] J.M. Nascimento, J. Dias, Vertex component analysis: a fast algorithm to unmix hyperspectral data, IEEE Trans. Geosci. Remote Sens. 43 (4) (2005) 898–910.
[14] J.M. Bioucasdias, A variable splitting augmented Lagrangian approach to linear spectral unmixing, Proc. 1st Workshop Hyperspectr. Image Signal Process.: Evol. Remote Sens. (WHISPERS09), 2009, pp. 1–4.
[15] M. Iordache, J.M. Bioucas-Dias, A. Plaza, Collaborative sparse regression for hyperspectral unmixing, IEEE Trans. Geosci. Remote Sens. 52 (1) (2013) 341–354.
[16] M. Iordache, J.M. Bioucas-Dias, A. Plaza, Total variation spatial regularization for sparse hyperspectral unmixing, IEEE Trans. Geosci. Remote Sens. 50 (11) (2012) 4484–4502.
[17] J.W. Boardman, Automating spectral unmixing of AVIRIS data using convex geometry concepts, Proc. AVIRIS Workshop., 1993, pp. 11–14.
[18] M.E. Winter, N-FINDR: An algorithm for fast autonomous spectral end-member determination in hyperspecral data, Proc. SPIE Conf. Imag. Spectr. V. 3753 (1999) 266–275.
[19] V. Pauca, J. Piper, R.J. Plemmons, Nonnegative matrix factorization for spectral data analysis, Linear Algebra Appl. 416 (1) (2006) 29–47.
[20] S. Jia, Y. Qian, Constrained nonnegative matrix factorization for hyperspectral unmixing, IEEE Trans. Geosci. Remote Sens. 47 (1) (2009) 161–173.
[21] Z. Yang, G. Zhou, S. Xie, S. Ding, J. Yang, J. Zhang, Blind spectral unmixing based on sparse nonnegative matrix factorization, IEEE Trans. Image Process. 20 (4) (2011) 1112–1125.
[22] Y. Qian, S. Jia, J. Zhou, A. Robles-Kelly, Hyperspectral unmixing via $\ell_{1/2}$ sparsity-constrained nonnegative matrix factorization, IEEE Trans. Geosci. Remote Sens. 49 (11) (2011) 4282–4297.
[23] N. Wang, B. Du, L. Zhang, An endmember dissimilarity constrained non-negative matrix factorization method for hyperspectral unmixing, IEEE J. Sel. Topics Appl. Earth Observ. Remote Sens. 6 (2) (2013) 554–569.
[24] D.L. Donoho, V. Stodden, When does non-negative matrix factorization give a correct decomposition into parts?, Proc. Adv. Neural Inf. Process. Syst. (2003) 1141–1148.
[25] W. He, H. Zhang, L. Zhang, Sparsity-regularized robust non-negative matrix factorization for hyperspectral unmixing, IEEE J. Sel. Topics Appl. Earth Observ. Remote Sens. 9 (9) (2016) 4267–4279.
[26] F. Zhu, Y. Wang, S. Xiang, B. Fan, C. Pan, Structured sparse method for hyperspectral unmixing, ISPRS J. Photogramm. Remote Sens. 88 (2014) 101–118.
[27] W. He, H. Zhang, L. Zhang, Total variation regularized reweighted sparse nonnegative matrix factorization for hyperspectral unmixing, IEEE Trans. Geosci. Remote Sens. 55 (7) (2017) 3909–3921.
[28] W. Wang, Y. Qian, Y.Y. Tang, Hypergraph-regularized sparse NMF for hyperspectral unmixing, IEEE J. Sel. Topics Appl. Earth Observ. Remote Sens. 9 (2) (2016) 681–694.
[29] H. Wang, W. Yang, N. Guan, Cauchy Sparse NMF with manifold regularization: A robust method for hyperspectral unmixing, Knowl.-Based Syst. 184 (2019) 104898.
[30] H. Gao, Y. Yang, S. Lei, C. Li, H. Zhou, X. Qu, Multi-branch fusion network for hyperspectral image classification, Knowl.-Based Syst. 167 (2019) 11–15.
[31] Y. Fan, C. Zhang, Z. Liu, Z. Qiu, Y. He, Cost-sensitive stacked sparse auto-encoder models to detect striped stem borer infestation on rice based on hyperspectral imaging, Knowl.-Based Syst. 168 (2019) 49–58.
[32] Y. Fang, H. Zhang, Y. Ren, Unsupervised cross-modal retrieval via multi-modal graph regularized smooth matrix factorization hashing, Knowl.-Based Syst. 171 (2019) 69–80.
[33] B. Pálsson, J. Sigurdsson, J. Sveinsson, M. Ulfarsson, Hyperspectral unmixing using a neural network autoencoder, IEEE Access. 6 (2018) 25646–25656.
[34] Y. Qian, F. Xiong, S. Zeng, J. Zhou, Y. Tang, Matrix-vector nonnegative tensor factorization for blind unmixing of hyperspectral imagery, IEEE Trans. Geosci. Remote Sens. 55 (3) (2017) 1776–1792.
[35] F. Xiong, Y. Qian, J. Zhou, Y.Y. Tang, Hyperspectral unmixing via total variation regularized nonnegative tensor factorization, IEEE Trans. Geosci. Remote Sens. 57 (4) (2019) 2341–2357.
[36] X. Zhao, W. Wang, T. Zeng, T. Huang, M.K. Ng, Total variation structured total least squares method for image restoration, SIAM J. Sci. Comput. 35 (6) (2013) B1304–B1320.
[37] T.G. Kolda, B.W. Bader, Tensor decompositions and applications, SIAM Rev. 51 (3) (2009) 455–500.
[38] USGS, USGS Digital spectral library 06, 2016, Available-online: https://aviris.jpl.nasa.gov/data/free_data.html.
[39] M. Iordache, J.M. Bioucas-Dias, A. Plaza, Collaborative sparse regression for hyperspectral unmixing, IEEE Trans. Geosci. Remote Sens. 52 (1) (2014) 341–354.
[40] S. Paris, P. Kornprobst, J. Tumblin, F. Durand, Bilateral filtering: Theory and applications, Found. Trends Comput. Graph. Vis. 4 (1) (2008) 1–73.
[41] Y. Zheng, G. Liu, S. Sugimoto, S. Yan, M. Okutomi, Practical low-rank matrix approximation under robust L1-norm, in: IEEE Conf. Comput. Vis. Pattern Recognit. (CVPR), 2012, pp. 1410–1417.
[42] S. Gu, Q. Xie, D. Meng, W. Zuo, X. Feng, L. Zhang, Weighted nuclear norm minimization and its applications to low level vision, Int. J. Comput. Vis. 121 (2017) 183–208.
[43] Y. Chen, W. He, N. Yokoya, T. Huang, Hyperspectral image restoration using weighted group sparsity-regularized low-rank tensor decomposition, IEEE Trans. Cybern. 50 (8) (2020) 3556–3570.
[44] J. Yang, X. Zhao, T. Ji, T. Ma, T. Huang, Low-rank tensor train for tensor robust principal component analysis, Appl. Math. Comput. 367 (2020) 124783.
[45] J. Wright, A. Ganesh, S. Rao, Y. Peng, Y. Ma, Robust principal component analysis: Exact recovery of corrupted low-rank matrices via convex optimization., Proc. Adv. Neural Inf. Process. Syst. 1 (2009) 2080–2088.
[46] P.V. Giampouras, K.E. Themelis, A.A. Rontogiannis, K. Koutroumbas, Simultaneously sparse and low-rank abundance matrix estimation for hyperspectral image unmixing, IEEE Trans. Geosci. Remote Sens. 54 (8) (2016) 4775–4789.
[47] R. Wang, W. Liao, H. Li, H. Zhang, A. Pizurica, Hyperspectral unmixing by reweighted low rank and total variation, in: Proc. Workshop Hyperspectral Image Signal Process., Evol. Remote Sens., 2016, pp. 1–4.
[48] J. Huang, T. Huang, L. Deng, X. Zhao, Joint-sparse-blocks and low-rank representation for hyperspectral unmixing, IEEE Trans. Geosci. Remote Sens. 57 (4) (2019) 2419–2438.
[49] J. Xu, K. Xu, K. Chen, J. Ruan, Reweighted sparse subspace clustering, Comput. Vis. Image. Underst. 138 (2015) 25–37.
[50] J. Huang, T.-Z. Huang, X.-L. Zhao, L.-J. Deng, Nonlocal tensor-based sparse hyperspectral unmixing, IEEE Trans. Geosci. Remote Sens. (2020) http://dx.doi.org/10.1109/TGRS.2020.3030233.
[51] Q. Qu, N.M. Nasrabadi, T.D. Tran, Abundance estimation for bilinear mixture models via joint sparse and low-rank representation, IEEE Trans. Geosci. Remote Sens. 52 (7) (2014) 4404–4423.
[52] S. Gu, L. Zhang, W. Zuo, X. Feng, Weighted Nuclear Norm Minimization with Application to Image Denoising, in: IEEE Conf. Comput. Vis. Pattern Recognit. (CVPR), 2014, pp. 2862–2869.
[53] W. Dong, G. Shi, X. Li, Y. Ma, F. Huang, Compressive sensing via nonlocal low-rank regularization, IEEE Trans. Image Process. 23 (8) (2014) 3618–3632.
[54] D.D. Lee, H.S. Seung, Algorithms for non-negative matrix factorization, in: Proc. 13th Int. Conf. Neural Inf. Process. Syst., 2000, pp. 556–562.
[55] D. Bertsekas, Nonlinear programming, in: Athena Scientific, Second Edition, Belmont, MA, 1999, pp. 02178–9998.
[56] C.J. Lin, On the convergence of multiplicative update algorithms for nonnegative matrix factorization, IEEE Trans. Neural Netw. 18 (6) (2007) 1589–1596.
[57] E. Gonzalez, Y. Zhang, Accelerating the Lee-Seung algorithm for non-negative matrix factorization, Tech. Rep., Dept. Comput. Appl. Math., Rice Univ., Houston, TX, USA, 2005, pp. 1–13.
[58] S. Zhang, j. Li, Z. Wu, A. Plaza, Spatial discontinuity-weighted sparse unmixing of hyperspectral images, IEEE Trans. Geosci. Remote Sens. 56 (10) (2018) 5767–5779.
[59] J. Huang, T. Huang, X. Zhao, L. Deng, Joint-sparse-blocks regression for total variation regularized hyperspectral unmixing, IEEE Access 7 (2019) 138779–138791.
[60] F. Zhu, Y. Wang, B. Fan, S. Xiang, G. Meng, C. Pan, Spectral unmixing via data-guided sparsity, IEEE Trans. Image Process. 23 (12) (2014) 5412–5427.
[61] F. Zhu, Y. Wang, B. Fan, G. Meng, C. Pan, Effective Spectral Unmixing via Robust Representation and Learning-based Sparsity., in: arXiv: Proc. Int. Conf. Comput. Vis. Pattern Recognit. (CVPR), 2014.
[62] AVIRIS, AVIRIS jasper data, 2014, Available-online:http://www.escience.cn/system/file?fileId=68574.
[63] HYDICE, HYDICE urban data, 2014, Available-online:http://www.escience.cn/system/file?fileId=68574.